Black hole feeding and star formation in NGC 1808

Audibert, A.; Combes, F.; García-Burillo, S.; Hunt, L.; Eckart, A.; Aalto, S.; … ; Martín, S.

Smoking-gun evidence of black hole feeding in NGC 1808

A. Audibert[1,2], F. Combes[1,3], S. García-Burillo[4], L. Hunt[5], A. Eckart[6], S. Aalto[7], V. Casasola[8], F. Boone[9], M. Krips[10], S. Viti[11,12], S. Muller[7], K. Dasyra[13], P. van der Werf[11], and S. Martín[14,15]

[1] Observatoire de Paris, LERMA, PSL University, Sorbonne University, CNRS, Paris, France
  e-mail: anelise.audibert@obspm.fr
[2] National Observatory of Athens (NOA), Institute for Astronomy, Astrophysics, Space Applications and Remote Sensing (IAASARS), GR–15236, Greece
[3] Collège de France, 11 Pl. Marcelin Berthelot, 75231, Paris
[4] Observatorio Astronómico Nacional (OAN-IGN)-Observatorio de Madrid, Alfonso XII, 3, 28014 Madrid, Spain
[5] INAF - Osservatorio Astrofisico di Arcetri, Largo E. Fermi, 5, 50125, Firenze, Italy
[6] I. Physikalisches Institut, Universität zu Köln, Zülpicher Str. 77, 50937, Köln, Germany
[7] Department of Space, Earth and Environment, Chalmers University of Technology, Onsala Space Observatory, SE-43992 Onsala, Sweden
[8] INAF - Istituto di Radioastronomia, via Piero Gobetti 101, 40129, Bologna, Italy
[9] CNRS, IRAP, 9 Av. colonel Roche, BP 44346, 31028, Toulouse Cedex 4, France
[10] IRAM, 300 rue de la Piscine, Domaine Universitaire, F-38406 Saint Martin d'Hères, France
[11] Leiden Observatory, Leiden University, PO Box 9513, 2300 RA Leiden, Netherlands
[12] Dep. of Physics and Astronomy, UCL, Gower Place, London WC1E 6BT, UK
[13] Dep. of Astrophysics, Astronomy & Mechanics, Faculty of Physics, National and Kapodistrian University of Athens, Panepistimiopolis Zografou, 15784, Greece, and National Observatory of Athens, Institute for Astronomy, Astrophysics, Space Applications and Remote Sensing, Penteli, 15236, Athens, Greece
[14] European Southern Observatory, Alonso de Córdova, 3107, Vitacura, Santiago 763-0355, Chile
[15] Joint ALMA Observatory, Alonso de Córdova, 3107, Vitacura, Santiago 763-0355, Chile

ABSTRACT

We report ALMA observations of CO(3-2) emission in the Seyfert2/starburst galaxy NGC 1808, at a spatial resolution of 4 pc. Our aim is to investigate the morphology and dynamics of the gas inside the central 0.5 kpc, and to probe nuclear feeding and feedback phenomena. We discovered a nuclear spiral of radius 1 " = 45pc and inside it a decoupled circumnuclear disk, or molecular torus of radius 0.13" = 6pc. The HCN(4-3) and HCO$^+$(4-3) and CS(7-6) dense gas line tracers were simultaneously mapped and detected in the nuclear spiral and present the same misalignment in the molecular torus. At the nucleus the HCN/HCO$^+$ and HCN/CS ratios indicate the presence of an AGN. The molecular gas shows regular rotation, within a radius of 400 pc, except for the misaligned disk inside the nuclear spiral arms. The computations of the torques exerted on the gas by the barred stellar potential reveal that the gas within a radius of 50 pc is feeding the nucleus, on a time-scale of ~ 60 Myr. Some non-circular motions are observed towards the center, corresponding to the nuclear spiral arms. We cannot rule out that small extra kinematic perturbations could be interpreted as a weak outflow due to the AGN feedback. The molecular outflow detected at ⩾250 pc in the NE direction is likely due to supernovae feedback and it is connected to the kpc scale superwind.

Key words. Galaxies: active – Galaxies: starburst – Galaxies: Individual: NGC 1808 – Galaxies: ISM – Galaxies: kinematics and dynamics – Galaxies: nuclei

1. Introduction

The physical processes to feed galaxy nuclei at the 10 pc-scale are still not yet well known, but the advent of ALMA (the Atacama Large Millimeter Array) has recently opened new windows to trace the molecular gas at high resolution and sensitivity (García-Burillo et al. 2014, 2016; García-Burillo et al. 2019; Combes et al. 2019; Alonso-Herrero et al. 2019). Bars and nuclear bars were already hinted at dynamical mechanisms (Shlosman et al. 1989) and confirmed at kpc down to 100 pc-scale (Combes 2001; García-Burillo & Combes 2012), and recently nuclear bars acting on gaseous nuclear spirals have been observed to be very efficient at 10 pc-scale (Combes et al. 2014; Audibert et al. 2019). The goal is now to find more cases to con-

firm this mechanism. The high spatial resolution is also pivotal to discover AGN feedback and distinguish it from supernovae feedback (Cicone et al. 2014; Feruglio et al. 2015; Salak et al. 2016). In many galaxies, both occur simultaneously (Rupke et al. 2005; Veilleux et al. 2013; Dasyra et al. 2014), but winds and molecular outflows starting at radii below the 10 pc scale would point towards AGN feedback.

In this paper, we present ALMA observations in the CO(3-2) line of the Starburst/Seyfert 2 NGC 1808, with a spatial resolution up to 4 pc. Its proximity (9.3 Mpc) and moderate inclination of 57° make NGC 1808 an ideal target to test and refine scenarios of AGN feeding and feedback, and potentially discover new phenomena controlling gas structures and dynamics within 400 pc, where the dynamical time-scale is smaller than ~ 10 Myr
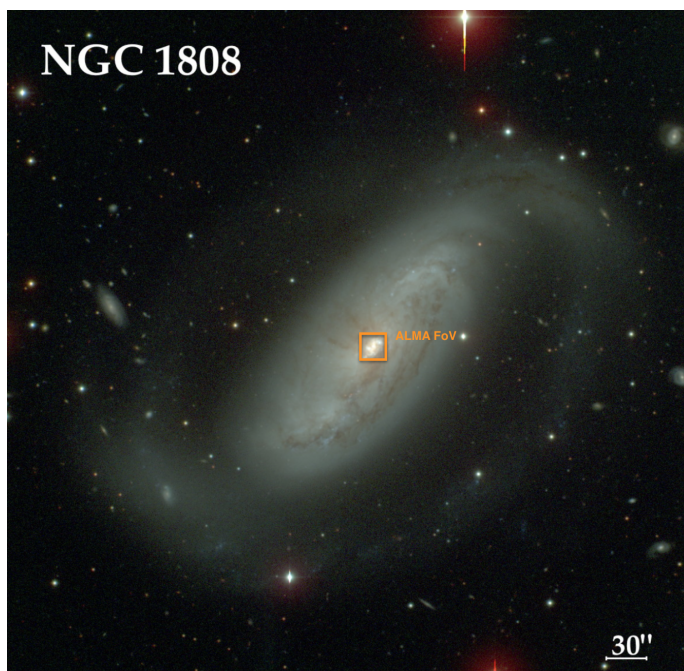
Fig. 1. Large scale (8.9'×8.9') optical image of NGC 1808 obtained with the 2.5-meter Irénée du Pont telescope at Las Campanas Observatory. The ALMA 18″ FoV is shown in the orange square for comparison. Credits: Carnegie-Irvine Galaxy Survey (Ho et al. 2011).

(for Vrot=200 km/s). In the next subsection, all relevant characteristics of NGC 1808 are described. Observations are detailed in Section 2 and results in Section 3. The interpretation in term of torques is discussed in Section 4, and conclusions are drawn in Section 5.

1.1. NGC 1808

The galaxy NGC 1808 is remarkable for its very dusty appearance and especially for its well-known system of dark radial filaments; it has also dust lanes perpendicular to the disk, parallel to the minor axis, up to 3 kpc from the major axis. It is known for its peculiar nuclear region of "hot spots" (Sérsic & Pastoriza 1965). NGC 1808 is a Starburst/Sy 2 galaxy located at 9.3 Mpc (1″=45 pc) and it is classified as an SAB(s)a. According to Reif et al. (1982), it has an inclination of 57° and a PA=323° in the optical (Dahlem et al. 1990). In Figure 1, a large scale (8.9'×8.9') optical image of the galaxy obtained with the Carnegie-Irvine Galaxy Survey (CGS) is shown (Ho et al. 2011). Atomic gas traced with H I is concentrated in the galactic bar, disk, and a warped outer ring, indicating a tidal interaction in the past with the neighbour galaxy NGC 1792 (Koribalski et al. 1996). The prominent polar dust lanes correspond to gas outflow emerging from the nucleus, as revealed in optical studies that indicate an outflow of neutral and ionised gas, as seen in Hα, [N II], Na I D and H I by Koribalski et al. (1993a); Phillips (1993). In particular, Na I D is seen blueshifted in absorption and redshifted in emission and *B-R* images show that the dust plumes associated with the outflow reach ~3 kpc above the plane. NGC 1808 has been classified as a superwind galaxy, similar to M 82, due to the evidence of large-scale outflows, likely due to the starburst (Dahlem et al. 1990, 1994). Near-infrared integral-field spectroscopy with SINFONI by Busch et al. (2017) showed a large gas reservoir and a disturbed gas velocity field that shows signs of inflowing

Table 1. Properties of NGC 1808

Parameter	Value	Reference
αJ2000[a]	05h07m42.34s	(1)
δJ2000[a]	-37d30m46.98s	(1)
V_{hel}	995 kms^{-1}	(1)
RC3 Type	SAB(s)a	(2)
Nuclear Activity	Sy 2/ Starburst	(1,3)
Inclination	57°	(4)
Position Angle	311°	(5)
Distance[b]	9.3 Mpc	(1)
SFR[c]	4.7 M$_\odot$yr^{-1}	(1)
M_{HI}	3.4×10^9 M$_\odot$	(4)
M_* - Stellar Mass	2.1×10^{10} M$_\odot$	(6)
M_{H2}	2×10^9 M$_\odot$	(5)
L_{IR}	5.1×10^{10}L$_\odot$	(7)
αJ2000[d]	05h07m42.33s	(8)
δJ2000[d]	-37d30m45.88s	(8)

Notes. References: 1: NASA/IPAC Extragalactic Database (NED); 2: (de Vaucouleurs et al. 1991); 3: Veron-Cetty & Veron (1986); 4: Reif et al. (1982); 5: Dahlem et al. 1990; 6: Combes et al. (2019); 7: (Sanders et al. 2003); 8: this work.
[a] (α_{J2000}, δ_{J2000}) is the phase tracking center of our interferometric observations.
[b] Distance is the median values of z-independent distances from NED Steer et al. (2017)
[c] SFR is derived from infrared luminosity (NED)
[d] The RA-DEC positions are the new adopted center, derived from the central continuum peak in this work, with an uncertainty of ~0.1" (see Sec. 3.1)

streaming motion in the central ~100 pc. The main properties of NGC 1808 are summarised in Table 1.

2. Observations

NGC1808 was observed with the ALMA in several array configurations, covering the CO(3-2), CS(7-6), HCN(4-3), and HCO$^+$ lines in band 7 with a final combined resolution of 0.27″(~12 pc). We present the summary of the observations below and in Table 2.

First, in ALMA cycle 3 (project ID: #2015.1.00404.S, PI F. Combes), NGC 1808 was observed simultaneously in CO(3-2), HCO$^+$(4-3), HCN(4-3) and CS(7-6) for both the compact (TC, baselines 15 to 612m) and the extended (TE, baselines 15 to 1462 m) configurations. The TC configuration was observed in April 2016 with 42 antennas and an on source integration time of 4 minutes, providing a synthesized beam of ~0″.36. The TE configuration was observed in August 2016 with 38 antennas, on source integration of 20 minutes and a synthesized beam of ~0″.14. The correlator setup, designed to simultaneously observe the four lines, provided a velocity range of 1600 km/s for each line, but did not center the HCO$^+$(4-3) and HCN(4-3) lines (200 km/s on one side and 1400 km/s on the other, which is adequate for a nearly face-on galaxy), and 1800 MHz bandwidth in the continuum.

Then, in ALMA Cycle 4 the observations (project ID:#2016.1.00296.S, PI F. Combes) were performed in November 2016 and August 2017 at higher spatial resolution (~4 pc) aiming at resolving the molecular torus. The tuning configura-

Table 2. Observations summary.

Date	N_{ant} [a]	B_{min} / B_{max} [b] (m / km)	θ_{res} [c] ('')	$LRAS$ [d] ('')	PWV [e] (mm)	t_{on} [f] (min)
21 Apr 2016 [g]	42	15 / 0.6	0.36	3.9	0.8	4
12 Aug 2016 [g]	38	15 / 1.5	0.14	2.7	0.4	20
26 Nov 2016 [h]	42	15 / 0.7	0.31	2.7	0.4	11
03 Aug 2017 [h]	44	21 / 3.6	0.07	0.8	0.6	35

Notes: (a) Number of 12 m-antennas in the array; (b) Respectively minimum and maximum projected baseline; (c) Synthesized beam with this configuration alone; (d) Largest recoverable angular scale; (e) Amount of precipitable water vapor in the atmosphere; (f) On-source time; (g) ALMA project number 2015.1.00404.S; (h) ALMA project number 2016.1.00296.S.

tion of Band 7 was in the CO(3-2), HCO$^+$(4-3) and continuum, providing a broader spectral window centered at the emission line. The correlator setup was selected to center the CO(3-2) and the HCO$^+$ lines in the 2 GHz bandwidth. The compact configuration (TM2, baselines 15 to 704 m) was observed with 42 antennas for an integration time of 11 minutes and a synthesized beam of 0.''31 and the extended (TM1, baselines 21 to 3638m) with 44 antennas for 35 minutes on source and a synthesized beam of 0.''07.

The observations were centred on the nucleus, with a single pointing covering a field-of-view (FoV) of 18''. The galaxy was observed in dual polarization mode with 1.875 GHz total bandwidth per spectral window, and a channel spacing of 0.488 MHz corresponding to ~0.8 km/s, after Hanning smoothing. The flux calibration was done with radio quasars (J0522-3627, J0519-4546, J0453-3949) close to the position in the sky of the target, which are regularly monitored at ALMA, and resulted in about 10% accuracy.

The data from Cycle 3 and 4 were calibrated and concatenated with the CASA software (version from 4.5.3 to 4.7.2, (McMullin et al. 2007), and the imaging and cleaning were performed with the GILDAS software (Guilloteau & Lucas 2000). The analysis were made in GILDAS together with PYTHON packages (radio-astro-tools, APLpy, PySpecKit Ginsburg et al. 2015; Robitaille & Bressert 2012; Ginsburg & Mirocha 2011). The spectral line maps were obtained after subtraction of the continuum in the uv-plane using the tasks UV_CONTINUUM and UV_SUBTRACT. Differently than in the paper presenting the data by Combes et al. (2019), where we have used only the most extended configurations (TM1+TE), in this work we have combined all the configurations. In the case of the emission line datacubes, the CLEANing was performed using the Hogbom method and a natural weighting, excluding he TM1 configuration (due to very high noise outside the nuclear region) in order to achieve the best sensitivity, resulting in a synthesized beam of 0.''30×0.''24 for the concatenated data cube. The data cubes were then smoothed to 10.16 km/s (11 MHz). For the continuum maps, we selected the line emission free channels and concatenated all the configurations (TE+TC+TM1+TM2), and we provide two images according to resolution: the $contA$ map, using natural weighting, yielding a synthesized beam of 0.''2 and $contB$ using uniform weighting and achieving a better angular resolution, with a synthesized beam size of 0.''08 (~4 pc). The total integration time provided an rms of 57μJy/beam in the continuum, and in the line channel maps 0.35 mJy/beam per channel of 10 km/s. The final maps were corrected for primary beam attenuation. Very little CO(3-2) emission was detected outside the full-width half-power (FWHP) primary beam.
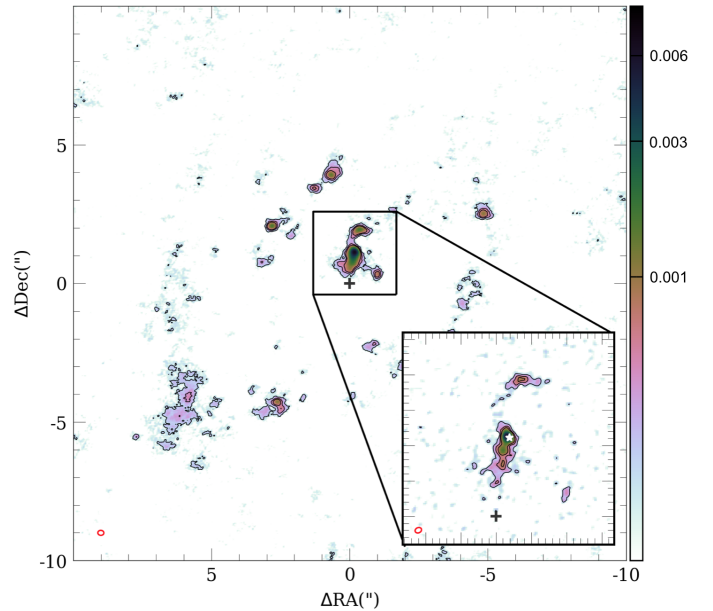

Fig. 2. Continuum emission at 0.87 mm. The central 20''×20'' is shown in the main panel for the natural weighting image ($contA$). The red ellipse at the bottom left corner indicates the synthesized beam size of 0.22''×0.18''at PA=86°. The contours are 3, 5 and 9 times the σ_{rms}. The zoom-in of the central 3''×3'' at high resolution (0.09''×0.07''at PA=115°, $contB$) is shown in the right bottom corner. The black cross indicates the adopted phase center, while the white star represents the peak of the continuum emission, assumed to be the AGN position (see Table 1). The colour scale is in Jy/beam.

3. Results

3.1. Continuum emission

Radio continuum emission in NGC 1808 was reported by Collison et al. (1994) using 3.6 cm radio observations with the Very Large Array (VLA). They found a family of compact radio sources along the ring in the central region of the galaxy, and the nuclear component has a flux of 62.8 mJy. Comparing to the VLA measurements at 6 cm of Saikia et al. (1990), the spectral indices of the compact sources in the ring are consistent with almost all of them being supernova remnants (SNRs) or H II regions. In the nuclear core, ALMA band 3 observations at ~93 GHz and 2.6''resolution found a spectral index $\alpha_{nuc} \sim -1$ (Salak et al. 2016, 2017), typical of synchrotron emission. They suggested that the nuclear region is dominated by a high-energy source, e.g., supernova explosions and/or a low luminosity AGN (LLAGN). The results are consistent with the findings of Dahlem
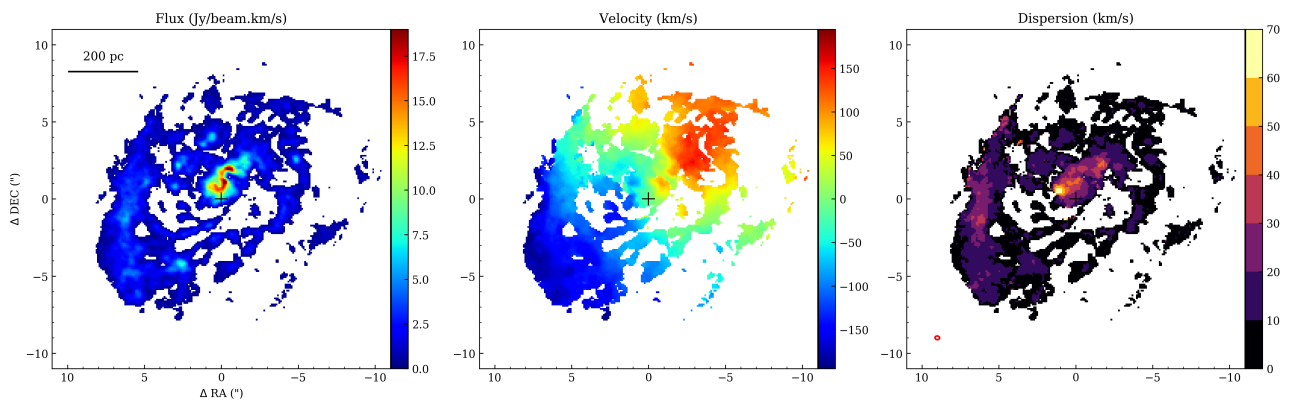
Fig. 3. CO(3-2) moments maps of NGC 1808 in the central 22" (∼1 kpc). *Left:* integrated intensity map (0*th* moment) of CO(3-2). *Middle:* mean velocity (1st moment) and *right:* velocity dispersion (2nd moment. The synthesized beam is indicated as the red ellipse in the bottom left corner of the velocity dispersion map.

et al. (1990), who measured a spectral index of α_{nuc}=-0.9 from 20 and 6 cm radio images.

Our 0.87 mm continuum observation in band 7 at 0.2″resolution (*contA*) is shown in Figure 2. We find a nuclear component and some compact regions along the ring. In the zoomed panel at the bottom right, we show the continuum at higher resolution (4 pc, *contB*). The white star in the figure indicates the peak of the continuum emission, adopted as the AGN position, listed in Table 1. The continuum is a point source inside the nuclear spiral and may also correspond to a torus, of radius 0.13″=6 pc (Combes et al. 2019).

In the nuclear region compared to the 3.6 cm VLA observations, we also find that the 0.87 mm continuum is consistent with synchrotron emission. At the nuclear "spot", the 3.6 cm radio continuum presented in Collison et al. (1994) has a peak flux of 8.96 mJy/beam for a resolution of 0.62"×0.53" and at the same position, the integrated flux is 39.2 mJy in a 2" diameter aperture (Kotilainen et al. 1996). At 350 GHz, the higher resolution continuum map, *contB*, shows a maximum in flux of S_{peak}(*contB*)=3.51 mJy/beam and the 0.22"×0.18" continuum map, *contA*, has S_{peak}(*contA*)=6.78 mJy/beam. By taking into account the peak fluxes, the spectral index to the 3.6 cm VLA radio continuum is α_{nuc}=-0.25 and -0.07, for the *contB* and *contA*, respectively. Additionally, we smoothed our 350 GHz continuum map at the same resolution of the 3.6 cm radio continuum. The integrated flux in a 2" diameter region around the AGN position leads to a flux density of $S_{0.87mm}$=27.8 mJy, which allows us to compare to the value of $S_{3.6cm}$=39.2 mJy reported by Kotilainen et al. (1996) and to obtain a spectral index of α_{nuc}=-0.09.

Towards higher frequencies, since we approach the Rayleigh–Jeans regime of the dust emission, we expect to have more contribution from the cold dust and therefore to have spectral indices between α ∼3–4. The continuum at 500 GHz observed with ALMA in Band 8 at 0.825"×0.59"resolution is presented by Salak et al. (2019). At the AGN position, the continuum peaks at 54 mJy and smoothing our 350 GHz continuum at the same resolution of the 500 GHz map, we have a flux peak of $S_{0.87mm}$=14.9 mJy we derive an index of α=3.6.

3.2. Molecular gas distribution and morphology

In the Appendix, we present the channel maps for the CO(3-2) observations. Figure B.1 displays 40 of the CO(3-2) channel maps, with a velocity range of 400 km/s and a velocity resolution of 10.2 km/s. The channels show evidence of a regular

velocity field in a patchy ring at a radius ∼7″(315 pc), that is most prominent in the south part and another broken ring at ∼3.5″(160 pc). They are connected by multiple spiral arms. Inside the star-forming ring at 3.5″, that is also detected in the ionised and H_2 gas by Busch et al. (2017), at the very center, a 2-arm spiral structure is clearly seen, that is also observed in CS, HCN and HCO$^+$, as we will further discuss in Section 3.5.

The moment maps of the CO(3-2) line (clipping the emission at <5σ_{rms}) are shown in Figure 3. The integrated intensity (zero-moment) map in the left panel of Figure 3 shows that the CO emission follows the ∼300 pc star-forming circumnuclear ring. Salak et al. (2016) and Salak et al. (2017) have mapped the CO(1-0) and CO(3-2) emission with ALMA at resolution of 1″17×0″77 and 1″04×0″56 respectively. They also detected molecular spiral arms, and a 500 pc pseudo-ring, however, they have called "molecular torus" a double peak structure at radius 30 pc and a circumnuclear disk in the central 100 pc. At our higher spatial resolution, this double peak interpreted as a torus is actually the 2-armed nuclear spiral evidently seen in the central 100 pc. The evidence of inflowing gas through this trailing spirals will be discussed in Section 4.4. We also find a torus in a smaller compact structure, of radius 6 pc, inside the nuclear spiral (Combes et al. 2019).

Figure 4 shows the CO(3-2) contours superposed onto the *HST* maps in the F658N filter[1]. The CO and optical maps show a remarkable similarity in morphology; the molecular ring seen in the CO emission coincides with the dusty nuclear ring in the HST image, and the winding arms are the beginning of the characteristic dust lanes along the bar.

In the middle panel of Figure 3, the intensity-weighted velocity (first-moment) map shows a clear rotation pattern in the galaxy plane, with velocities peaking between $-200 < v < 150$ km/s from the systemic velocity (v_{sys}=995 km/s). We see also clearly that there is nuclear circumnuclear kinematically decoupled from the larger disk, in which the position angle is being tilted from 311 to close to 270°. Close to the AGN position, the velocity dispersion is about (σ ∼40 km/s), as displayed in the right panel of Figure 3 (second-moment map). Along the nuclear spiral the velocity dispersion ranges from 20∼66 km/s and the average dispersion along the ring is ∼10 km/s. Also, we can distinguish a disturbance in the southeast part of the external ring, with an increased dispersion ≳35 km/s.

---

[1] The HST image was aligned to the ALMA astrometry, the peak emission in the HST image was re-centered to the AGN position in Table 1. The resolution is 0.05 "/pixel.
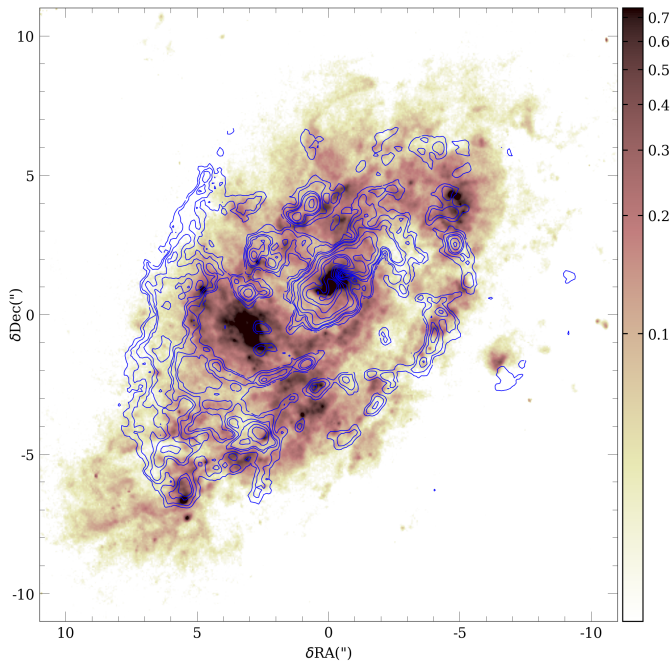
Fig. 4. WFC/F658N HST image and the CO(3-2) contours overlaid.

3.3. CO luminosity and H_2 mass

In order to estimate the missing flux, we compare the ALMA observations to the central spectrum obtained with the 15-m single dish obtained with the Swedish-ESO Submillimeter Telescope (SEST) in CO(1-0) and CO(2-1) over a 43″ and 22″ FoV, respectively. In Figure A.1, we display the total CO(3-2) spectrum integrated over the 18″FoV. Towards the central position, Aalto et al. (1994) found a CO(2-1) spectrum peaking at T_{mb}= 0.84 K with FWHM=268 km/s, yielding a total integrated flux of 227 K.km/s (4751 Jy.km/s), in a beam of 22″. Their beam is very similar to our FoV of 18″, therefore, we can compare the fluxes since both FoV's encompasses the entire nuclear ring.

We assume a brightness temperature ratio of $r_{32} = T_{3-2}/T_{2-1}$ of 0.66±0.02 and $r_{21} = T_{2-1}/T_{1-0} = 1.12±0.01$, derived from the SEST CO(2-1)/CO(1-0) observations in the galaxy center, by convolving the beam of CO(2-1) to 43″, which implies a higher CO excitation at the center of NGC 1808. This is expected for thermalized excitation and a dense molecular medium. In that case, the CO(3-2) flux should be higher than the CO(2-1), as we could presume the flux $S_\nu \propto \nu^2$ in the Rayleigh-Jeans approximation, for gas at temperature larger than 25 K and density larger than 10^4 cm^{-3}:

$$S_\nu(Jy) = \frac{2\kappa T_B}{c^2}\nu^2\Theta_s^2 = \frac{2.65}{\lambda^2(cm^2)}T_B(K)\Theta_s^2(arcmin) \quad (1)$$

Using these values, the expected CO(3-2) intensity is ~4723 Jy.km/s in a 18″ beam. When integrated over the spectral range ($v \sim \pm200$ km/s), the integrated emission in our ALMA FoV of 18″ shown in Figure A.1, is 2594 Jy.km/s. Therefore, we should expect some missing flux by a factor up to ~40-50%, taking into account the uncertainties of the r_{32} and r_{21} ratios (deconvolution uncertainties were not taken into account in Aalto et al. 1994).

The mass of molecular can be estimated from the integrated flux $S_{CO}\Delta V$ using the equation from Solomon & Vanden Bout

(2005):

$$L_{CO}'(K.km/s/pc^2) = 3.25 \times 10^7 \frac{S_{CO}\Delta V}{1+z}\left(\frac{D_L}{\nu_{rest}}\right)^2 \quad (2)$$

where ν_{rest} is the rest frequency of the observed line, in GHz, D_L is the luminosity distance, in Mpc, z is the redshift and $S_{CO}\Delta V$ is the integrated flux in Jy.km/s. The molecular mass then can be calculated using the CO-to-H_2 conversion factor $M(H_2) = \alpha_{CO}r13L_{CO}'$.

We find a CO luminosity of L_{CO}' =6.1×10^7 K.km/spc^2 and molecular mass of 2.7×10^{8}M$_\odot$ in our FoV, assuming a Milky-Way like CO-to-H_2 conversion factor of X_{CO} = 2×10^{20} cm^{-2}/(K.km/s) (e.g. Bolatto et al. 2013). In comparison, Dahlem et al. (1990) derived a total molecular mass of $M_{H2} \approx 2×10^9$ M$_\odot$ using the SEST CO(1-0) observations in the central 43″ beam and standard conversion factor (Table 1). For the values of SEST CO(2-1) spectrum in the central 22″ beam reported by Aalto et al. (1994), it gives a mass of 1×10^9 M$_\odot$ for a CO(2-1)/CO(1-0) ratio of 1.12. The M_{H2} estimates from Dahlem et al. (1990) and Aalto et al. (1994) are consistent and the rather smaller values derived with the ALMA high resolution observations are due to the missing flux (~50%) of lacking single-dish observation to detect weak extended emission.

The total CO(3-2) emission line profile integrated over the observed map (FoV of 18″) is shown in Figure A.1. We decomposed the spectrum in three velocity components, C1, C2 and C3, and the results of the Gaussian fits for each component are displayed in Table A.1. The total flux is $S_{CO(3-2)}$=2594.4 Jy.km/s.

3.4. CO(3-2) kinematics

To derive the CO(3-2) kinematics, we have assumed a simple model for the rotation curve, proposed by Bertola et al. (1991), that considers that the gas is on circular orbits in a plane, $v_c = Ar/(r^2+c^2)^{p/2}$, where for $p = 1$ the velocity curve is asymptotically flat and $p = 3/2$ the system has a finite total mass, therefore we expect $1 \leq p \leq 3/2$. The observed radial velocity at a position (R, Ψ) on the plane of the sky can be described as:

$$v(R, \Psi) = v_{sys} + \quad (3)$$
$$\frac{ARcos(\Psi - \Psi_0)sin(\theta)cos^p(\theta)}{\{R^2\left[sin^2(\Psi - \Psi_0) + cos^2(\theta)cos^2(\Psi - \Psi_0)\right] + c^2cos^2(\theta)\}^{p/2}}$$

where θ is the inclination of the disk (with $\theta = 0$ for a face-on disk), Ψ_0 is the position angle of the line of nodes, v_{sys} is the systemic velocity and R is the radius and A, c, and p are parameters of the model.

From the velocity map, the dominant velocity feature appears to be due to circular rotation in the disk. We used the tilted-ring model (Rogstad et al. 1974), which consists in dividing the velocity field in concentric rings in radii Δr and each ring is allowed to have an arbitrary v_c, i and PA. For each radius, we can independently fit the parameters of Equation 3 to the observed velocity field. We show the results of the tilted-ring fitting to the velocity map in Figure 5. We adopted a Δr=0″.3, that corresponds to the de-projected resolution of our observations in the galaxy plane. In the right panel, we display the residuals after subtracting the tilted-model ring to the velocity field. As can be seen in Fig. 5, the tilted-ring represents very well the observed velocity field, with small amplitude values in the residuals
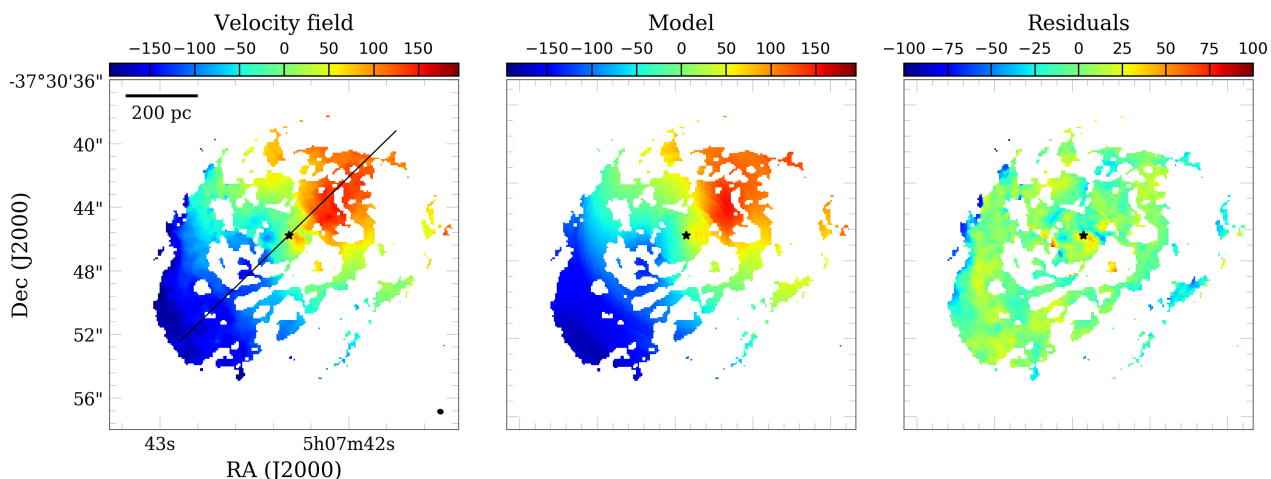
Fig. 5. *Left:* Velocity map of NGC 1808 clipped at $>5\sigma$. In the *middle* panel the best fit using the tilted-ring model Rogstad et al. (1974) and the residuals, after subtracting the model from the data, are shown on the *right*. The straight line in the left panel represents the kinamatical PA=314° of the major axis derived from the best fit.

(± 30 km/s), indicating that mean velocity field is well described by rotation.

We also tested an additional method to derive the CO kinematics, using the "3D-Based Analysis of Rotating Objects from Line Observations" (^{3D}BAROLO) software by Di Teodoro & Fraternali (2015). ^{3D}BAROLO performs a 3D tilted-ring modeling of the emission line data-cubes to derive the parameters that better describe the kinematics of the data. We ran ^{3D}BAROLO on the CO(3-2) data-cube in order to investigate non-circular motions, since the code allows us to infer radial velocities in the fit of the rotation curves.

We investigate the position-velocity diagrams (PVDs) along the major (PA=314°) and minor axis (224°) of NGC 1808 (Fig. 6), to detect a possible outflow feature which would correspond to the polar dust lanes. Our CO(3-2) observations along the minor axis reveal that the bulk of the molecular gas corresponds to the nuclear spiral arms, source of important non-circular motions. Within the central arcsecond, there exists high-velocity gas (100-200km s^{-1}) which is associated to the spiral arms, with the same morphology. We cannot exclude the presence of a weak outflow along the minor axis, within this one arcsec (45 pc) radius from the center, but it is not possible to quantify it. Outside a radius of one arcsec, velocities are mainly due to circular rotation and some perturbations from co-planar streaming motions along the spirals arms. In the very center (6 pc), there is a velocity gradient likely due the fact that the kinematic is perturbed because of the decoupling of the torus, in which we observe a change in the PA. We discuss this misalignment in Section 4.3.

Salak et al. (2016, 2017) presented evidence of a molecular gas outflow seen in CO(1-0) with ALMA from the nuclear starburst region (r$\lesssim$250 pc) of NGC 1808 that could be only detected in the PVDs. The outflow has a maximum de-projected velocity of $v_{out} \sim 180$ km/s and mass outflow rate between 1-10 M$_\odot$/yr, comparable to the total star formation rate in the starburst 500 pc region, that corresponds to SFR$\sim$5M$_\odot$/yr in the "hot spots". Our results are compatible with this.

3.5. Dense gas: HCO$^+$, HCN and CS emission

As mentioned before, the tuning configuration of the observations allowed us to observe the high density gas tracers HCN(4-
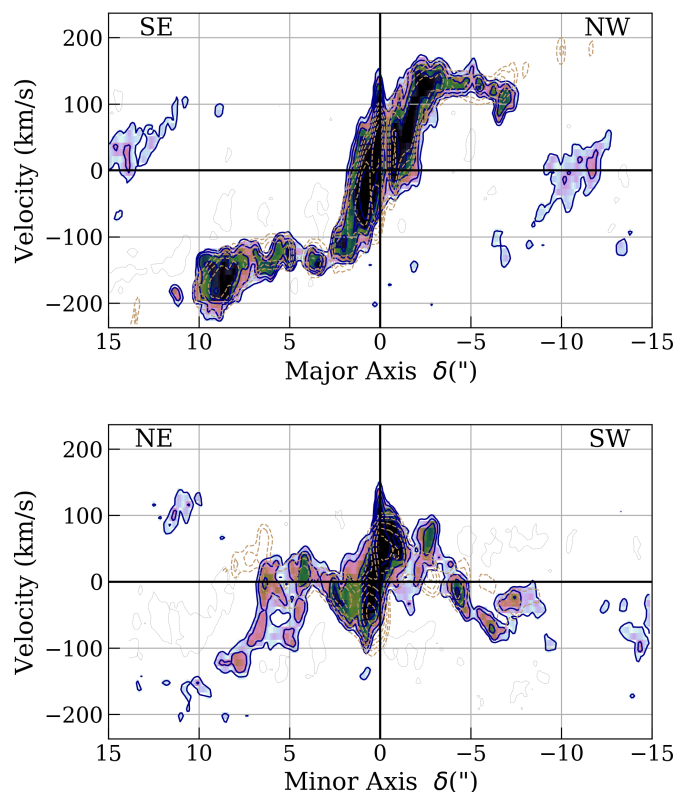

Fig. 6. Position-velocity diagrams of NGC 1808 along the major axis at a PA=314° (*top panel*) and minor axis (PA=224°, *bottom*). We used a 0″.3 slit width. The dashed lines are the best fit from ^{3D}BAROLO.

3), HCO$^+$(4-3) and CS(7-6). The detection of these transitions is shown in Figure 7. The 2-arm nuclear spiral traced by CO(3-2) is also visible in HCN(4-3), HCO+ (4-3), and CS(7-6) maps.

Regarding the ambiguous Starburst/AGN nature of NGC 1808, the presence of a weak AGN is still debatable. Based on the Hα/[N$_{II}$]=0.94$\pm$0.05 line ratio classification of Veron-Cetty & Veron (1986), NGC 1808 is classified as a Seyfert galaxy. Ginga X-ray data (1.5–37 keV) by Awaki & Koyama (1993) show evidence of an obscured AGN and it is attributed as Seyfert 2. However, other observational evidences
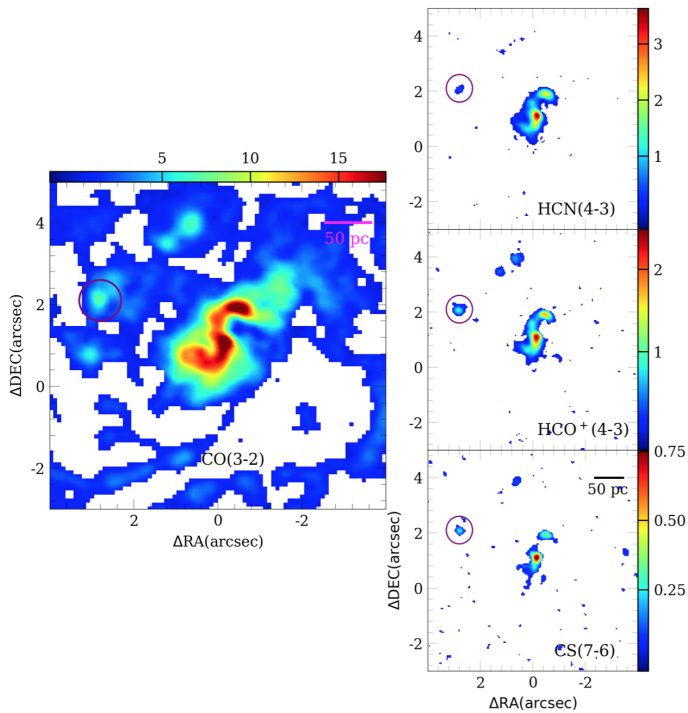
Fig. 7. *Left:* a zoomed 8"×8" region of CO(3-2) intensity map for NGC 1808 of Figure 3. *Right:* the integrated intensity maps of the dense gas tracers HCN(4-3), HCO$^+$(4-3) and CS(7-6) in the top, middle and bottom panels, respectively, in the same region. The purple circle indicates the position of a clump detected in the HCN, HCO$^+$ and CS.

Table 3. Line ratios: R_{HCN/HCO^+} and $R_{HCN/CS}$

Region	R_{HCN/HCO^+}	$R_{HCN/CS}$
AGN	2.96±0.44	9.78±1.47
Clump (3σ)	0.27±0.04	1.63±0.24
Clump (5σ)	0.09±0.01	0.59±0.09

Notes. Ratios of the HCN, HCO$^+$ ans CS lines in the CND region and in the clump shown in Fig. 7.

point to the starburst nature of the excitation mechanism in NGC 1808 (Phillips 1993; Dopita et al. 2015). *XMM-Newton* and *Chandra* observations by Jiménez-Bailón et al. (2005) indicate the co-existence of a starburst component along with a LLAGN contribution in the nucleus.

Thanks to our high-resolution ALMA observations we are able to disentangle the emission coming from the nuclear region within the spiral trailing feature observed in the central ∼50 pc and the contribution from a star-forming clump observed in all the molecular tracers at ∼150 pc from the nucleus, indicated in Figure 7. We measured the line intensity ratios R_{HCN/HCO^+} and $R_{HCN/CS}$ in the two regions, and plot in the submillimeter-HCN diagram (Fig. 8) proposed by Izumi et al. (2016), which suggest enhanced HCN(4-3)/HCO$^+$(4-3) and/or HCN(4-3)/CS(7-6) integrated intensity ratios in circumnuclear molecular gas around AGNs compared to those in starburst galaxies (submillimeter HCN-enhancement). Indeed, we do find that the nuclear region of NGC 1808 presents excitation conditions typical of X-ray dominated regions (XDRs) in the vicinity of AGNs, supporting the idea/evidence of the presence of an AGN in the nucleus of NGC 1808.
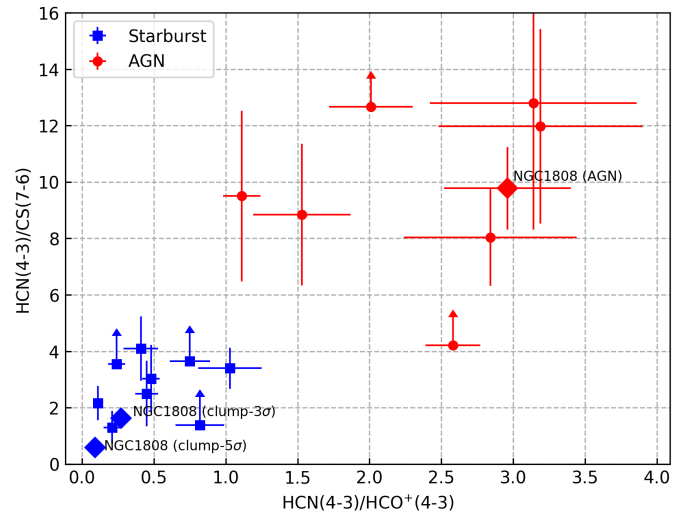

Fig. 8. The submillimeter-HCN diagram proposed by Izumi et al. (2016) for the high-resolution observations (spatial resolution <500 pc) using the line intensity ratios R_{HCN/HCO^+} and $R_{HCN/CS}$. The red circles represent the AGNs and the blue squares indicate the SB galaxies. We include the line ratios of NGC 1808 (diamonds) measured in the central spiral, called here as "AGN" and in a clump detected ∼150 pc north-west of central position in all the dense tracers.

4. Discussion

4.1. The ionised and warm molecular gas

In order to compare the CO(3-2) morphology with the ionised material and the warm molecular gas, we superposed on Figure 9 the CO contours onto the NIR maps obtained with SIN-FONI of Paα and H$_2\lambda$2.12μm presented in Busch et al. (2017). The SINFONI observations have a FoV of 8"×8" and a resolution of 0.125"/pixel, comparable to our ALMA observations (0.098"/pixel). There is a remarkable resemblance between the CO emission and the ionised and warm molecular gas along the star forming ring at ∼4″radius. This SF ring is better traced by radio continuum emission (Collison et al. 1994), Paα, and also the shock tracer [Fe II] than by the excited H$_2$ emission (Busch et al. 2017). It shows hot spots of star formation, corresponding to molecular cloud associations, of typical sizes 50 pc, composed of several molecular clouds, of sizes ranging from 5 to 10 pc, according to the resolution.

According to Salak et al. (2018), all molecular clouds along the SF ring have density and high HCN(1-0)/HCO$^+$(1-0) line ratio (of order ∼1), possibly indicating that the excitation mechanisms are from shocks, free–free emission from H II regions, and synchrotron emission from supernova remnants. This ratio even is higher towards the nucleus, with HCN/HCO$^+$ ∼1.5, which is consistent with the scenario of a composite starbust plus AGN (Privon et al. 2015; Salak et al. 2018). In addition, they also detected SiO(2-1), a shock tracer, only around the nuclear region of NGC 1808.

4.2. Resolved Kennicutt-Schmidt relation

Since we have high spatial resolution in the galactic center, both in star formation rate and gas surface density, it is possible to probe the Kennicutt-Schmidt (KS) resolved relation, even below the minimum scale of correlation (Schruba et al. 2010; Kruijssen et al. 2018). The regions considered for the comparison are in-
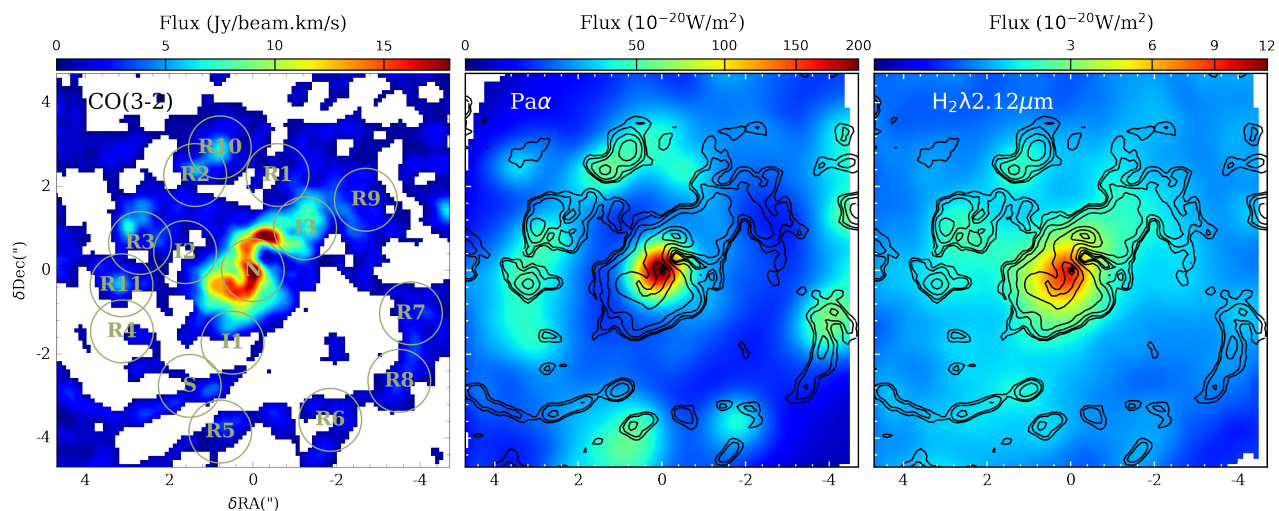
Fig. 9. Comparison between the CO(3-2) emission in the central 9″×9″ (left panel), with the Paα (*middle*) and H₂λ2.12µm (*right*) emission in the 8″×8″FoV of the SINFONI observations (Busch et al. 2017). The CO contours are overlaid in the NIR images. The black star represents the AGN position listed in Table 1. In the left panel 15 regions are identified, R1–R11, I1–I3 and N, to compute the Kennicutt-Schmidt relation of Fig 10.
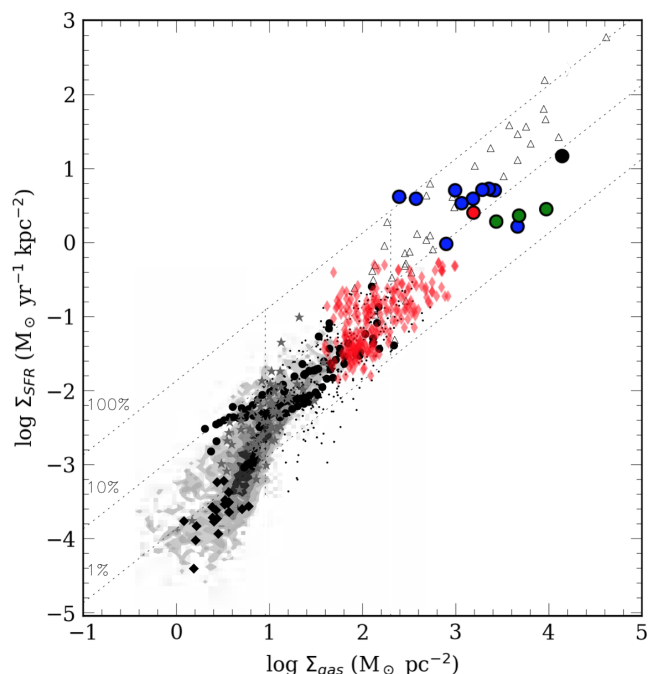

Fig. 10. Relation between the SFR and gas surface densities, in the 10 regions delimited in Figure 9. The nuclear region (N) is indicated by the black circle, the region along the circumm-nuclear ring (R1-R11) in blue, the south region (S) in red and in intermediate (I1-I3) regions in green. The NGC 1808 points are compared to the resolved KS relation from Bigiel et al. (2008) and the CO observations of the NUGA sample by Casasola et al. (2015, shown as the red diamonds).

Fig. 11. Depletion time, i.e. the ratio between gas and SFR surface densities, as a function of the aperture, or region in which it is computed. This defines a minimum region size of ∼ 500 pc, to apply the resolved KS relation. The average star and gas peaks models are from Schruba et al. (2010).

dicated in the left panel of Figure 9. The obtained relation is plotted in Figure 10.

To better compare the ionized and molecular gas distribution, we compute the surface densities of star formation rate (SFR) and molecular gas, to build a resolved Kennicutt-Schmidt (KS) diagram. We first considered the same region of star formation identified by Busch et al. (2017), although we know that they are biased towards H II regions, and then consider some peaks of the CO(3-2) emission, that are not remarkable in SFR, namely
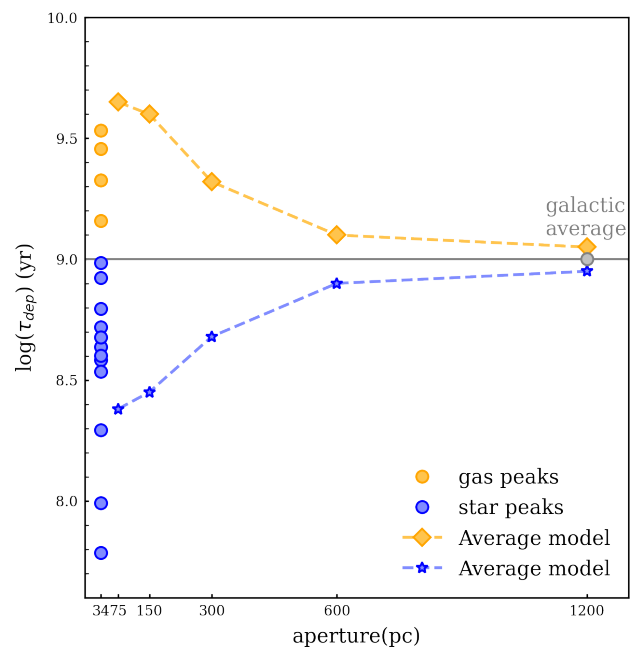
R8, R9, R10, R11 and I3 in Figure 9. The apertures used by Busch et al. (2017) where of radius 0.75″= 34 pc, and we follow with the same sizes, for the sake of comparison. In their work, they derived the cold gas mass from the warm H₂ gas detected at 2.12µm, with a conversion factor between warm and cold molecular hydrogen given by the ratio of $M_{H_2(cold)}/M_{H_2(warm)}$=0.3-1.6×10⁶, which is highly uncertain. The SFR in the our additional regions were computed using the Paα emission line corrected by the Calzetti et al. (2000) the extinction law and the

calibration of Panuzzo et al. (2003):

$$SFR_{Pa\alpha} = \frac{L(Pa\alpha)}{1.98 \times 10^{33} W} M_\odot \text{yr}^{-1} \qquad (4)$$

With masses estimates from our CO map, the resulting KS diagram is shown in Figure 10. We compare our findings with the work from Bigiel et al. (2008) that studied the star formation laws at sub-kpc scales in a sample of nearby galaxies and the work of Casasola et al. (2015) using HST and CO observations of the NUGA sample. All our points lie in the KS plane, but they present higher values of gas and SFR surface densities than the ones presented in Bigiel et al. (2008) and Casasola et al. (2015). Most of the regions along the ring (blue points in Fig. 10) present are located at the upper part of the KS plane, indicating high SF efficiencies, similar to starbursts galaxies (Kennicutt 1998). On the other hand, the intermediate regions I1-I3 (marked as green circles) and R9 in the ring all show lower star formation efficiencies.

A possible explanation could be due to the bias of the apertures selection according to the stars or gas peaks. In order to address the effects of the resolution and aperture selection, in Figure 11 we show two series of points: the bias to find more SFR while the selection is done on the optical (star peaks), or more gas surface density, when the selection is done on the molecular clouds (gas peaks), is quite clear. The regions I1-I3 and R9 are defined as the gas peaks and correspond to the region with lower SF efficiencies in the KS relation. The result of the bias selection trend is translated into the depletion time, $\tau_{dep} = \frac{\Sigma_{gas}}{\Sigma_{SFR}}$, and we found that the gas peaks show higher depletion times than the star peaks. This effect has been well described already by Schruba et al. (2010), and in more details by Kruijssen et al. (2018): at small scale, lower than typically 500 pc, we expect that the young stars and their surrounding ionized gas dissociate from the molecular association where they were born. From this relation, it could be possible to derive several quantities, like the star formation efficiency at the GMC scale, the feedback efficiency in terms of outflow velocity and mass ejected, and its coupling efficiency to the molecular disk. However, we have not enough regions to apply this method, in the small field of view of SINFONI (8″ = 360 pc), relative to the seeing resolution, and we postpone this study to future more extended observations. A more detailed analysis on the resolved KS law and star formation efficiencies for all galaxies in the sample presented in Combes et al. (2019) is going to be addressed in a forthcoming paper.

4.3. The kinematic misalignment at the center of the nuclear spiral

As was seen already in the previous section, with the CO(3-2) velocity field, there is a tilt of the kinematic major axis towards the nucleus. ALMA observations of neutral atomic carbon, [CI], presented in Salak et al. (2019) at a spatial resolution of 0.82"×0.6" show a remarkable resemblance with the CO(3-2) morphology and kinematics. They also reveal this tilted kinematics in the center. This decoupling kinematic feature is the indication of a nuclear disk and can be seen even in the dense gas tracers. In Figure 12, the intensity and velocity moment maps of HCN(4-3), HCO$^+$(4-3) and CS(7-6) are shown. Focusing into the center, the tilt is now clearer. The spirals arms tend to follow the same kinematics than the main disk. But towards the nucleus, there is a decoupled circum-nuclear disk, or molecular torus. This nuclear disk does not have the same kinematical PA than the galaxy disk (314°), but is tilted by about 30° towards
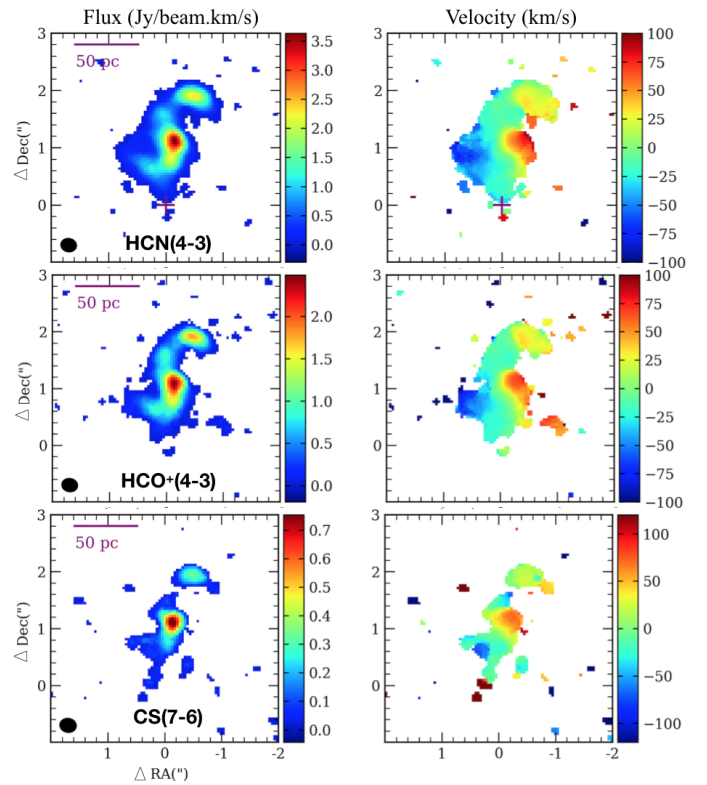

Fig. 12. The moment maps of the central emission of HCN(4-3), HCO$^+$(4-3) and CS(7-6) (from *top* to *bottom*). The synthesized beam sizes are show in the bottom left corner of the zero-moment map of each line. The purple cross is the phase of the observations.

280°. Such a kinematical decoupling is frequent and not unexpected (García-Burillo et al. 2019; Combes et al. 2019).

4.4. Inflowing of cold and warm molecular gas

The hot and cold gas, as well as the stellar velocity field, all show a very similar degree of rotation and therefore a simple residual map, which was obtained by subtracting the stellar velocity field from the velocity fields of both ionized gas traced by Brγ and warm molecular gas (traced by H$_2$) emission can provide us an estimate of the non-rotational motions in the gas velocity fields (Busch et al. 2017). The high spatial resolution (<50 pc) of SINFONI observations show evidence of a nuclear two-arm spiral structure in the central 100 pc (marked with solid lines in the residual maps presented in Figure 14 of Busch et al. (2017)).

Assuming that they are located within the disk plane and that the near side of the disc is in the south-west, Busch et al. (2017) concluded that the residual spiral arms could correspond to streaming motions towards the centre. The authors also compared the spiral arms with the optical HST/F614W map, and the possible inflow motions coincide with dust features.

The two-arm spiral structure detected in the residual maps of SINFONI observations are in remarkable coincidence with the nuclear spiral seen in our dense cold gas observations, giving additional support of the inflow of gas towards the nucleus of NGC 1808. The quantification of the amount of gas possibly fueling the nucleus is discussed in the following sections.

4.5. Lindblad resonances

NGC 1808 is a strongly barred late-type spiral galaxy, with typical dust lanes in the leading edges of the bar, the latter being also delineated by a series of HII regions all along 6 kpc (Koribalski et al. 1996). The 10″ radius CO ring (Salak et al. 2016, 2017) corresponds to a conspicuous ring in Hα, meaning that the gas is piling up in this ring and forms stars actively. This ring is likely the location of the inner Lindblad resonance. To check that, we have made a model of the rotation curve, to fit the observations of HI and Hα, adopting an inclination of the galaxy of 57°. We combined the different observations by Burbidge & Burbidge (1968), Saikia et al. (1990) and Koribalski et al. (1993b) adopting a common distance of D=9.3 Mpc (cf Fig. 13). We have placed the corotation at ∼1.4 bar radius, as usually found in numerical simulations and observations (O'Neill & Dubinski 2003). There exist two ILRs, around the location of the CO/Hα ring. The first one at radius 10″= 450 pc, certainly corresponds to the main ring of molecular gas condensation, and there exists a second ring, of ∼ 4-5″ radius, delineated by knots of radio continuum from supernovae, and called the star forming ring by Salak et al. (2018) (see their Figure 6, where the SF ring is delineated by central molecular clouds, CMC). This second ring is likely to correspond to the second ILR, at r=4.5″ or ∼ 200 pc.

Inside this ILR, the SINFONI K_s band measurements of Busch et al. (2017) have revealed a stellar nuclear bar, of 4″ radius. Its orientation is comparable, though slightly inclined with respect to the main bar of PA=145°, itself with an angle towards the kinematic major axis of the galaxy of PA=128°, determined from stellar kinematics (Busch et al. 2017). Either the nuclear bar is a prolongation of the main bar, with the same pattern speed, just slightly tilted due to the existence of the two ILR with perpendicular orbits (Combes 1994), or a secondary bar has decoupled from the main one, with a faster speed (Friedli & Martinet 1993). We favor the first possibility, since the orbital precessing rate $\Omega - \kappa/2$ shown in Fig. 13 is rather flat in the central kpc, allowing barely two ILRs. The conditions to trigger the decoupling of a secondary bar, as shown y simulations, are not yet fulfilled. The nuclear bar in the present configuration is the prolongation of the primary one; it can exert gravity torques on the gas, removing its angular momentum, and driving the gas to the center. In the next section, we present the calculations of these torques from the observations themselves.

4.6. Torque computation

To compute the stellar potential in the central kpc, and precisely inside a radius of 45 pc, the radius of the gaseous nuclear spiral, one of the best images would have been the HST image. However, the red HST image is highly obscured by dust, up to the point that it is not possible to see the nuclear bar. Instead, we chose to use the SINFONI K_s band image from Busch et al. (2017), with a field of view of 8"×8". To enlarge the field of view, we completed this image, with the VLT-VISTA K image, calibrating the borders to overlap with the same intensity. The final calibration is then obtained by the mass-to-light ratio, necessary to retrieve the observed rotation curve. According to the method described in Audibert et al. (2019), we de-project the NIR image, after subtracting a r=0.5″ spherical bulge, to a face-on view (with PA= 311° and i=57°), and resample both the derived potential and forces to the same grid as the CO(3-2) gaseous de-projected image, i.e. with a pixel of 0.085″= 3.8 pc. For this computation, we used the morphological center of the molecular nuclear spiral as reference. The gravitational potential is derived from
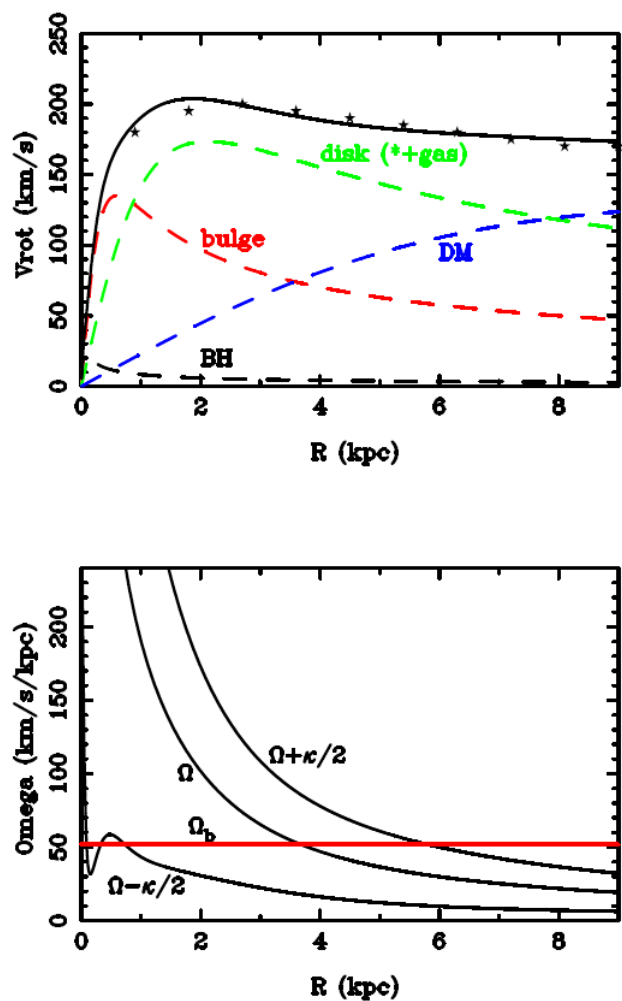

Fig. 13. Rotation curve model for NGC 1808. *Top*: An analytical model is built with 5 mass components, the stellar bulge and disk, the dark matter halo, the black hole and the gaseous disk. The two last ones contribute negligibly. The contribution of each component is indicated as a dashed line. The symbols are adapted from the observations of Hα and HI (Burbidge & Burbidge 1968; Saikia et al. 1990; Koribalski et al. 1993b). *Bottom*: The derived frequencies Ω, $\Omega \pm \kappa/2$, indicating the Lindblad resonances, with the pattern speed of the bar highlighted in red.

the stellar distribution, assuming a thin disk of scale ratio h_z/h_r =1/12, and solving the Poisson equation by the FFT method. We neglect the contribution of dark matter within a 1 kpc radius (the extent of this computation). At each pixel the torque exerted on the gas is computed, according to the procedure detailed in García-Burillo et al. (2005) or Combes et al. (2014) and plotted in Figure 14. In the top panel, the map of the gravitational torques shows a butterfly diagram (four-quadrant pattern) in relation to the nuclear bar orientation (PA$_{bar}$=128°) with torques changing sign as expected due to the barred potential.

Through azimuthal averaging, we derive the effective torque at each radius, per unit mass. Dividing by the average angular momentum at this radius (from the rotation curve), we obtain the relative rate of loss of angular momentum, as can be seen in Figure 15. The torque is negative in the nuclear spiral region, although it is relatively low. The gas is losing only 20-40% of its angular momentum in one rotation. The torque is positive in the region of the first and second ILR, and negative outside the ILR regions, meaning that the gas is maintained in the resonant rings,
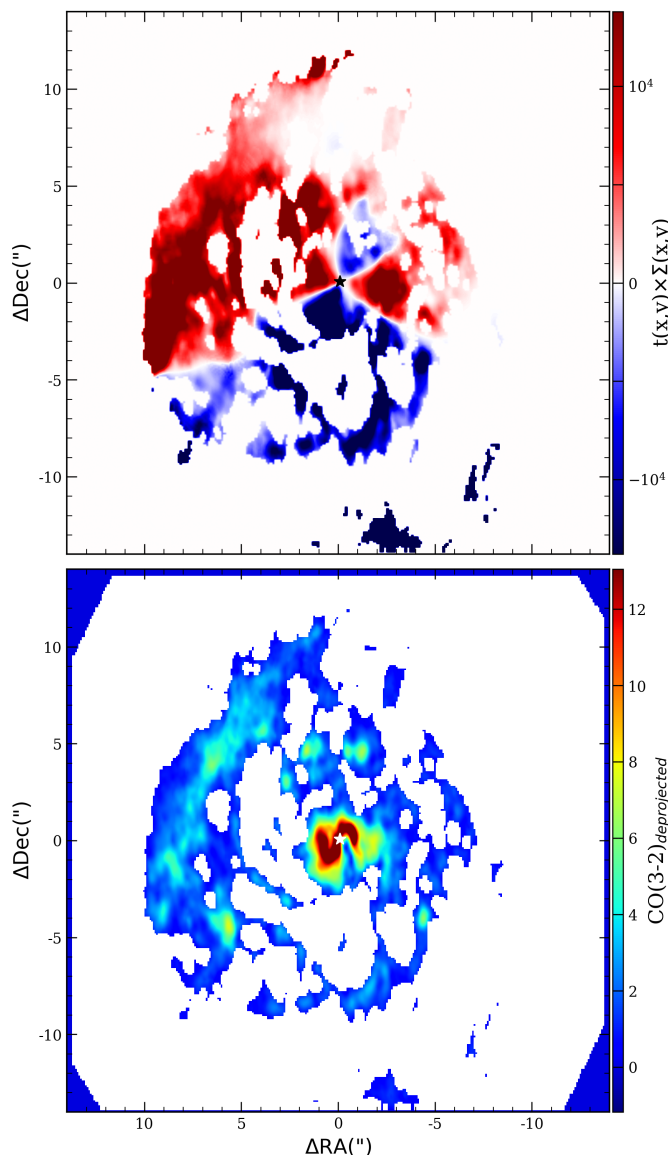
Fig. 15. The radial distribution of the torque, quantified by the fraction of the angular momentum transferred from the gas in one rotation– dL/L, estimated from the CO(3-2) de-projected map. The vertical dashed line at 6 pc radius delimitates the extent of the molecular torus, in this case unresolved to match the resolution of the NIR image. The torque is negative inside the ≲100 pc nuclear spiral and in the spiral arm at ~600 pc. Torques are positive in both ILRs and the filaments connecting them.

and evidence that the active nucleus is directly fed by the bar, due to a trailing nuclear spiral inside the ILR, and with in the sphere of influence of the black hole, has already been found in two other cases, NGC 1566 (Combes et al. 2014), NGC 613 (Audibert et al. 2019). Other smoking-gun evidence of fueling the galaxy center, although at a larger-scale, was obtained through other mechanisms, based on a decoupled secondary bar, as in NGC 2782 (Hunt et al. 2008). This case corresponds to a more evolved stage, where the nuclear bar evolution has weakened the primary bar into an oval.

5. Conclusion

The high spatial resolution and high sensitivity of ALMA band 7 observations of the Seyfert2/starburst galaxy NGC 1808 allow us to analyse the distribution and kinematics of the molecular gas within the central few hundreds parcsecs, showing evidence for feeding of the central SMBH. In addition to a central point source, corresponding to the AGN, the continuum emission is extended, with a steep spectral index corresponding to synchrotron emission. We interpret this extended emission as coming from the star formation in the nuclear spiral and clumps in the pseudo-ring, of radius $10'' = 450$ pc.

The CO(3-2) emission line cube revealed the morphology and dynamics of the gas inside the central 0.5 kpc: inside the pseudo-ring, tracing the first inner Lindblad resonance, we identified a second ILR of ~ 200 pc in radius. Inside this second ILR ring, all molecular lines reveal a very contrasted nuclear spiral of radius $1'' = 45$pc. This nuclear spiral is trailing, which is the configuration already encountered in two similar barred Seyferts, NGC 1566 and NGC 613 (Combes et al. 2014; Audibert et al. 2019). Trailing spirals are expected inside ILRs when the gas enters the sphere of influence of the central black hole.

The dense gas tracers, HCN(4-3), HCO$^+$(4-3) and CS(7-6) lines are also tracing clearly the nuclear spiral. We computed the gravitational potential due to a central nuclear bar, clearly

Fig. 14. *Top:* Map of the gravitational torque, t(x,y) × Σ(x,y), in the center of NGC 1808. The torques change sign as expected in a four-quadrant pattern (or butterfly diagram). The orientation of the quadrants follows the nuclear bar's orientation. In this de-projected picture, the major axis of the galaxy is oriented parallel to the horizontal axis. *Bottom:* The de-projected image of the CO(3-2) emission, at the same scale, and with the same orientation, for comparison.

which explains the hot spots of star formation there. Only in the very central region, under the gravitational influence of the black hole, the torque drives the gas towards the center.

As explained in Combes et al. (2014), without any gravitational influence of the central black hole, we could expect that the nuclear spiral structure is leading inside the inner ILR, and the torque positive. However, most of the gas of the nuclear spiral is within the sphere of influence of the black hole, which is 14 pc-36 pc according to the definition (Combes et al. 2019). The whole nuclear spiral is confined to a radius of 50 pc, and most of the central gas is imposing the trailing sense to the gas. This explains the negative torque, which drives the gas inwards. Figure 15 allows us to quantify the intensity of the torque, and the time-scale of the gas infall. We conclude that the gas is feeding the nucleus in a time-scale of ~60 Myr. This short time-scale,
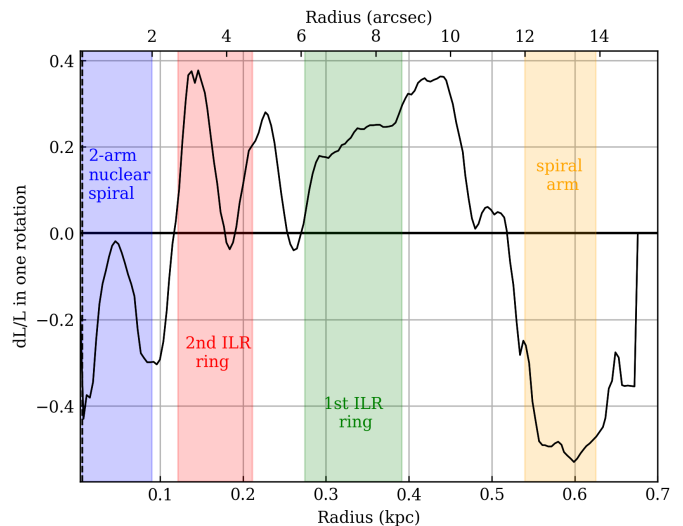
detected in the K-band image (Busch et al. 2017), with similar orientation as the primary bar. The torques exerted on the molecular nuclear spiral by the barred stellar potential reveal that the gas is feeding the nucleus, in a time-scale of 60 Myr.

Inside the nuclear spiral, the molecular gas appears kinematically decoupled in a tilted circum-nuclear disk of radius 0.13" = 6 pc, which is traced in CO(3-2) and also all dense gas tracers. This molecular disk or torus has HCN and HCO+ line ratios compatible with an excitation from the AGN. According to the distance from the center, the excitation changes progressively from AGN-like to starburst-like.

We searched for a possible molecular outflow in the nucleus, since this galaxy is known to host a large-scale superwind (Salak et al. 2016, 2017). The kinematics in the center is indeed perturbed within a radius of one arcsec (45 pc), showing a velocity gradient on the minor axis. These velocity perturbations follow the nuclear spiral morphology, and are interpreted as the associated non-circular motions. We cannot rule out a weak AGN-induced outflow. However, the more energetic large-scale outflow must be due to supernovae feedback from the known starburst.

References

Aalto, S., Booth, R. S., Black, J. H., Koribalski, B., & Wielebinski, R. 1994, A&A, 286, 365

Alonso-Herrero, A., García-Burillo, S., Pereira-Santaella, M., et al. 2019, A&A, 628, A65

Audibert, A., Combes, F., García-Burillo, S., et al. 2019, arXiv e-prints, arXiv:1905.01979

Awaki, H. & Koyama, K. 1993, Advances in Space Research, 13, 221

Bertola, F., Bettoni, D., Danziger, J., et al. 1991, ApJ, 373, 369

Bigiel, F., Leroy, A., Walter, F., et al. 2008, AJ, 136, 2846

Bolatto, A. D., Wolfire, M., & Leroy, A. K. 2013, ARA&A, 51, 207

Burbidge, E. M. & Burbidge, G. R. 1968, ApJ, 151, 99

Busch, G., Eckart, A., Valencia-S., M., et al. 2017, A&A, 598, A55

Calzetti, D., Armus, L., Bohlin, R. C., et al. 2000, ApJ, 533, 682

Casasola, V., Hunt, L., Combes, F., & García-Burillo, S. 2015, A&A, 577, A135

Cicone, C., Maiolino, R., Sturm, E., et al. 2014, A&A, 562, A21

Collison, P. M., Saikia, D. J., Pedlar, A., Axon, D. J., & Unger, S. W. 1994, MNRAS, 268, 203

Combes, F. 1994, in Mass-Transfer Induced Activity in Galaxies, ed. I. Shlosman, 170

Combes, F. 2001, in Advanced Lectures on the Starburst-AGN, ed. I. Aretxaga, D. Kunth, & R. Mújica, 223

Combes, F., García-Burillo, S., Audibert, A., et al. 2019, A&A, 623, A79

Combes, F., García-Burillo, S., Casasola, V., et al. 2014, A&A, 565, A97

Dahlem, M., Aalto, S., Klein, U., et al. 1990, A&A, 240, 237

Dahlem, M., Hartner, G. D., & Junkes, N. 1994, ApJ, 432, 598

Dasyra, K. M., Combes, F., Novak, G. S., et al. 2014, A&A, 565, A46

de Vaucouleurs, G., de Vaucouleurs, A., Corwin, Jr., H. G., et al. 1991, Third Reference Catalogue of Bright Galaxies. Volume I: Explanations and references. Volume II: Data for galaxies between 0^h and 12^h. Volume III: Data for galaxies between 12^h and 24^h.

Di Teodoro, E. M. & Fraternali, F. 2015, MNRAS, 451, 3021

Dopita, M. A., Shastri, P., Davies, R., et al. 2015, ApJS, 217, 12

Feruglio, C., Fiore, F., Carniani, S., et al. 2015, A&A, 583, A99

Friedli, D. & Martinet, L. 1993, A&A, 277, 27

García-Burillo, S. & Combes, F. 2012, in Journal of Physics Conference Series, Vol. 372, Journal of Physics Conference Series, 012050

García-Burillo, S., Combes, F., Ramos Almeida, C., et al. 2019, A&A, 632, A61

García-Burillo, S., Combes, F., Ramos Almeida, C., et al. 2016, ApJ, 823, L12

García-Burillo, S., Combes, F., Schinnerer, E., Boone, F., & Hunt, L. K. 2005, A&A, 441, 1011

García-Burillo, S., Combes, F., Usero, A., et al. 2014, A&A, 567, A125

Ginsburg, A. & Mirocha, J. 2011, PySpecKit: Python Spectroscopic Toolkit, Astrophysics Source Code Library

Ginsburg, A., Robitaille, T., Beaumont, C., et al. 2015, in Astronomical Society of the Pacific Conference Series, Vol. 499, Revolution in Astronomy with ALMA: The Third Year, ed. D. Iono, K. Tatematsu, A. Wootten, & L. Testi, 363–364

Guilloteau, S. & Lucas, R. 2000, in Astronomical Society of the Pacific Conference Series, Vol. 217, Imaging at Radio through Submillimeter Wavelengths, ed. J. G. Mangum & S. J. E. Radford, 299

Ho, L. C., Li, Z.-Y., Barth, A. J., Seigar, M. S., & Peng, C. Y. 2011, ApJS, 197, 21

Hunt, L. K., Combes, F., García-Burillo, S., et al. 2008, A&A, 482, 133

Izumi, T., Kohno, K., Aalto, S., et al. 2016, ApJ, 818, 42

Jiménez-Bailón, E., Santos-Lleó, M., Dahlem, M., et al. 2005, A&A, 442, 861

Kennicutt, Jr., R. C. 1998, ARA&A, 36, 189

Koribalski, B., Dahlem, M., Mebold, U., & Brinks, E. 1993a, A&A, 268, 14

Koribalski, B., Dahlem, M., Mebold, U., & Brinks, E. 1993b, A&A, 268, 14

Koribalski, B., Dettmar, R.-J., Mebold, U., & Wielebinski, R. 1996, A&A, 315, 71

Kotilainen, J. K., Forbes, D. A., Moorwood, A. F. M., van der Werf, P. P., & Ward, M. J. 1996, A&A, 313, 771

Kruijssen, J. M. D., Schruba, A., Hygate, A. e. P. S., et al. 2018, MNRAS, 479, 1866

McMullin, J. P., Waters, B., Schiebel, D., Young, W., & Golap, K. 2007, in Astronomical Society of the Pacific Conference Series, Vol. 376, Astronomical Data Analysis Software and Systems XVI, ed. R. A. Shaw, F. Hill, & D. J. Bell, 127

O'Neill, J. K. & Dubinski, J. 2003, MNRAS, 346, 251

Panuzzo, P., Bressan, A., Granato, G. L., Silva, L., & Danese, L. 2003, A&A, 409, 99

Phillips, A. C. 1993, AJ, 105, 486

Privon, G. C., Herrero-Illana, R., Evans, A. S., et al. 2015, ApJ, 814, 39

Reif, K., Mebold, U., Goss, W. M., van Woerden, H., & Siegman, B. 1982, A&AS, 50, 451

Robitaille, T. & Bressert, E. 2012, APLpy: Astronomical Plotting Library in Python, Astrophysics Source Code Library

Rogstad, D. H., Lockhart, I. A., & Wright, M. C. H. 1974, ApJ, 193, 309

Rupke, D. S., Veilleux, S., & Sanders, D. B. 2005, ApJ, 632, 751

Saikia, D. J., Unger, S. W., Pedlar, A., et al. 1990, MNRAS, 245, 397

Salak, D., Nakai, N., Hatakeyama, T., & Miyamoto, Y. 2016, ApJ, 823, 68

Salak, D., Nakai, N., Seta, M., & Miyamoto, Y. 2019, ApJ, 887, 143

Salak, D., Tomiyasu, Y., Nakai, N., et al. 2017, ApJ, 849, 90

Salak, D., Tomiyasu, Y., Nakai, N., et al. 2018, ApJ, 856, 97

Sanders, D. B., Mazzarella, J. M., Kim, D.-C., Surace, J. A., & Soifer, B. T. 2003, AJ, 126, 1607

Schruba, A., Leroy, A. K., Walter, F., Sand strom, K., & Rosolowsky, E. 2010, ApJ, 722, 1699

Sérsic, J. L. & Pastoriza, M. 1965, PASP, 77, 287

Shlosman, I., Frank, J., & Begelman, M. C. 1989, Nature, 338, 45

Solomon, P. M. & Vanden Bout, P. A. 2005, ARA&A, 43, 677

Steer, I., Madore, B. F., Mazzarella, J. M., et al. 2017, AJ, 153, 37

Veilleux, S., Meléndez, M., Sturm, E., et al. 2013, ApJ, 776, 27

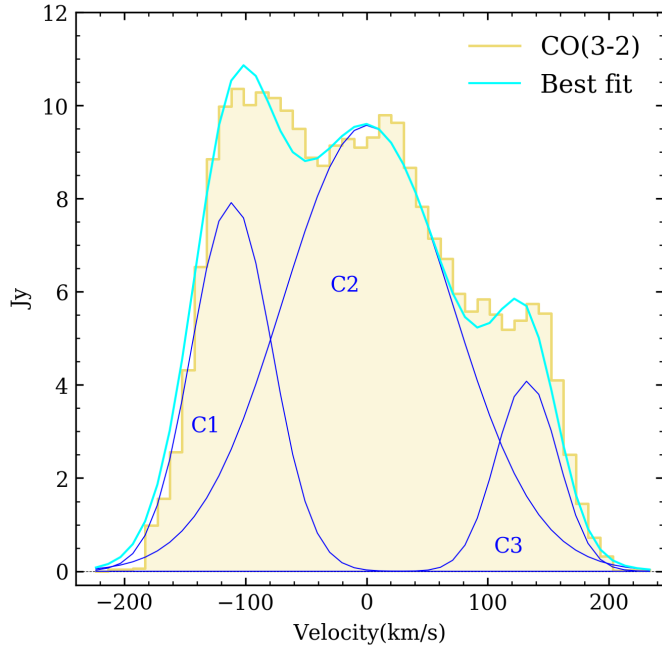Veron-Cetty, M.-P. & Veron, P. 1986, A&AS, 66, 335

Fig. A.1. We show the total CO(3-2) emission line profile integrated over the observed map, with a FOV of 18", after correction for primary beam attenuation. The light blue line is the result of the Gaussian fit with three velocity components (in dark blue); see Table A.1.

Table A.1. Line fluxes

Line	S_{CO} (Jy.km/s)	V (km/s)	ΔV^a (km/s)	S_{peak}^b (Jy)
C1	658.1 ± 113.8	-111.3 ± 1.7	78.1 ± 5.3	7.9
C2	1673.3 ± 187.6	0.5 ± 4.2	164.2 ± 15.8	9.6
C3	263.0 ± 53.7	132.5 ± 2.0	60.6 ± 6.2	4.1

Notes. Results of the Gaussian fits for the total CO(3-2) emission assuming the 3 velocity components (C1, C2 and C3), shown in Fig. A.1.
[a] Full width at half maximum (FWHM)
[b] Peak flux

Appendix A: Integrated spectrum and total mass estimation
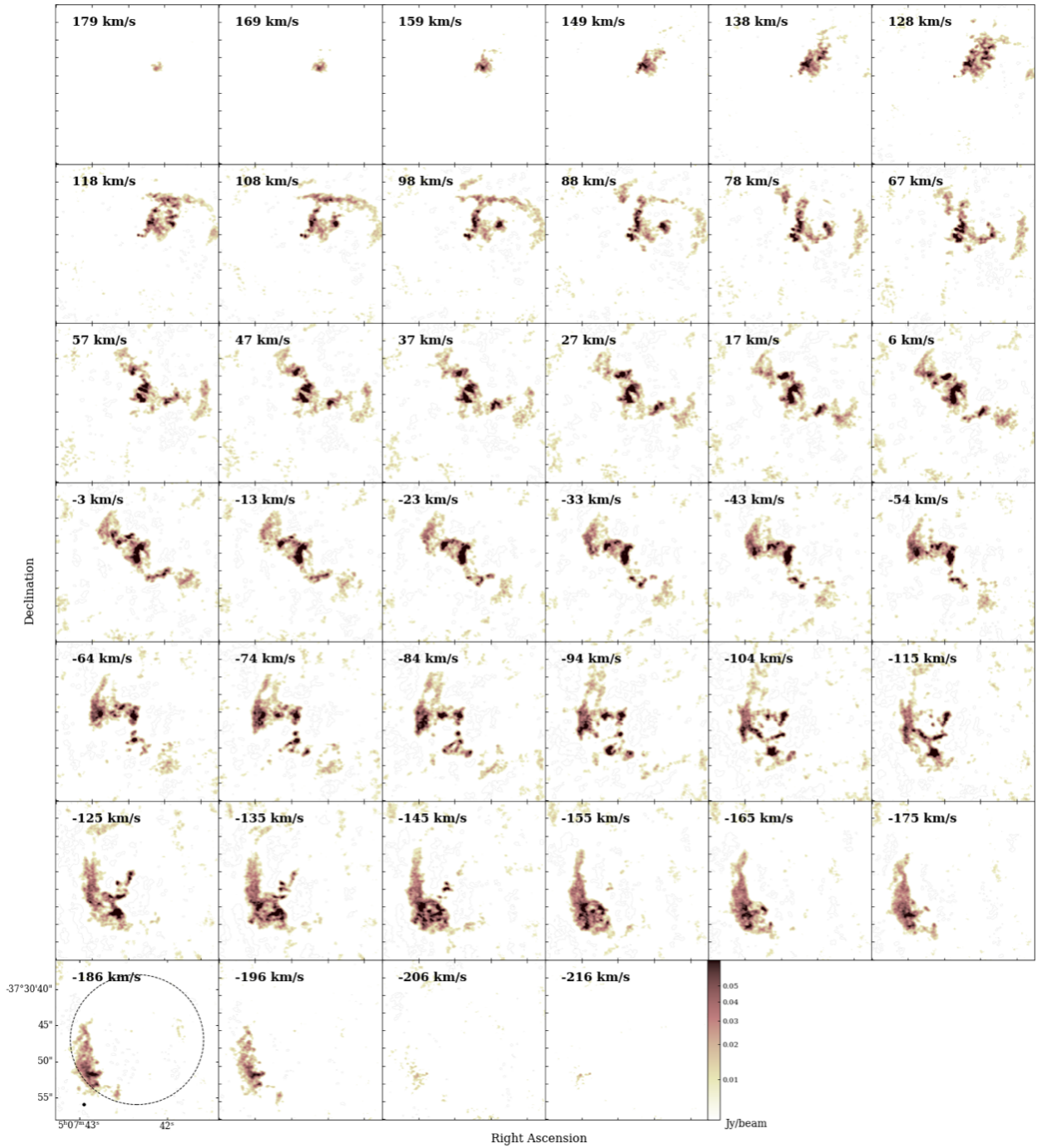
Appendix B: Channel maps

Fig. B.1. Channel maps of CO(3-2) emission in the centre of NGC 1808. Each of the 40 square boxes is 22" in size, while the primary beam is indicated by the dotted line in the bottom left panel. Channels are separated by 10.2km/s. They are displayed from 179 (top left) to -216 km/s (bottom right) related the $v(sys) = $kms^{-1}. The synthesized beam size is 0. 29"×0. 24" (PA=79.6°) and it is displayed as the black ellipse at the bottom left panel. The centre of the maps is the phase centre of the interferometric observations given in Table 1. The colour scale is in power stretch, ranging between 0 and 70 mJy/beam.